

Multiple Populations of Extrasolar Gas Giants

SHOHEI GODA¹ AND TARO MATSUO¹

¹Department of Earth and Space Science, Graduate School of Science, Osaka University, 1-1, Machikaneyamacho, Toyonaka, Osaka 560-0043, Japan

ABSTRACT

There are two planetary formation scenarios: core accretion and gravitational disk instability. Most extrasolar gaseous objects discovered to date are thought to be formed from the core accretion, based on a fact that gaseous objects are preferentially observed around metal-rich host stars. Here, we present the 623 samples in 520 planetary systems comprising gaseous planets and brown dwarfs discovered by radial velocity measurements in three mass regimes with boundary values of 4 and 20 Jupiter-mass in terms of the host-star metallicity through performing a cluster analysis to the samples, minimizing an impact of the selection effect of radial velocity measurements on the cluster analysis. The larger boundary is thought to be a boundary between planet and sub-stellar formations around G-type stars, being in agreement with the upper mass limit of the core-accreted planets predicted by some theoretical studies. The distributions of host-star metallicities, masses and eccentricities for the planetary objects lighter than 20 Jupiter-mass orbiting G-type stars can be naturally explained by the core accretion model. In contrast, the lower mass limit reflects a difference between planetary formation processes around early-type and G-type stars. A population with masses ranging from 4 to 20 Jupiter-mass orbiting early-type stars is thought to be composed of planets formed via the gravitational disk instability, considering that the population preferably orbits metal-poor stars or is independent of the host-star metallicity.

Keywords: methods: data analysis – planets and satellites: terrestrial planets

1. INTRODUCTION

Decades ago, the discussion of planetary formation in solar system was developed for the solar system (Hayashi et al. 1985). Two representative formation scenarios for Jupiter have been proposed: Core accretion (Perri & Cameron 1974; Mizuno 1980; Pollack et al. 1996) and disk instability (Kuiper 1951; Boss 1997; Mayer et al. 2002). In theory, the two planetary-formation processes have different dependences on disk metallicity, which is defined as the ratio of the metal-number-density to hydrogen atoms, and planet mass (e.g., Matsuo et al. 2007). For the core accretion model, a proto-planet core easily grows to the critical core mass before the disk gas dissipates. This occurs because the disk metallicity reflects the building materials available for the core (Ida & Lin 2004b; Mordasini et al. 2012). In fact, since the first planet orbiting a normal star was discovered (Mayor & Queloz 1995), large-sized radial velocity observations have revealed that, while the metallicities of stars hosting smaller planets such as Neptune-like planets and super-Earths are significantly lower than those of stars orbited by extrasolar gas giants (Mayor et al. 2011; Wang & Fischer 2015), the gas giants preferen-

tially orbit metal-rich stars (e.g., Santos et al. 2003; Fischer & Valenti 2005). Because the central star and its surrounding protoplanetary disks are formed from a same molecular cloud, according to the primordial hypothesis, most gas giants are thought to have formed via the core accretion. Regarding the planet mass, the gas giants with planet mass up to 30 M_J are potentially formed via the core accretion (e.g., Tanigawa & Ikoma 2007; Tanigawa & Tanaka 2016), where M_J represents Jupiter-mass. The number of the gas giants more massive than a few M_J gradually decreases as the planet mass is larger (e.g., Mordasini et al. 2009).

For the disk instability scenario, the relationship between disk metallicity and disk-instability-induced planetary formation has been theoretically studied; there exists reports of negative correlation (Cai et al. 2006; Durisen et al. 2007), a very weak positive correlation (Mayer et al. 2007), and no correlation (Boss 2002) in the metallicity range of the stars hosting the observed planets. Although the lower limit on the masses of the disk-instability-induced planets may exist (Matsuo et al. 2007), the mass distribution of the gas giants formed via the disk instability still remains an open question. On

the other hand, direct imaging of extrasolar planets orbiting HR8799, Formalhaut, and beta Pictoris reported in 2008 and 2010 (Marois et al. 2008; Kalas et al. 2008; Lagrange et al. 2010), respectively, confirmed the existing of outer planets, which can be naturally explained by the disk instability scenario rather than the extended core accretion with migration or planet-planet scattering (Dodson-Robinson et al. 2009). Thus, there may exist two populations originated from the two planetary formations.

Several previous studies (Ribas & Miralda-Escudé 2007; Santos et al. 2017) showed that the gas giants are divided into two regimes with a boundary mass of $4 M_J$ and interpreted the two populations as an outcome originated from the two planetary formations; while the gas giants lighter than $4 M_J$ are core-accreted planets, the gas giants more massive than $4 M_J$ are formed through disk instability. In addition, Schlaufman (2018) found that there is a transition between 4 and $10 M_J$ instead of a clear boundary of $4 M_J$ for gaseous objects orbiting G-type stars, performing a cluster analysis to a diagram of host-star metallicity and planet mass. However, it is possible to form very massive gas giants up to $30 M_J$ via the core accretion in theory (e.g., Tanigawa & Ikoma 2007; Mordasini et al. 2009; Tanigawa & Tanaka 2016) and the upper mass limit of the core-accreted planets is also expected to depend on the disk metallicity (Mordasini et al. 2012). Pebble accretion has been recently proposed as the third planetary formation scenario that enables massive core to be formed in the outer region beyond 10 AU (Ormel & Klahr 2010; Lambrechts & Johansen 2012); more massive planets than the core-accreted planets are potentially formed thanks to a wider Hill radius in more outer region. Thus, whether the boundary mass of $4 M_J$ or the transition between 4 and $10 M_J$ can be applied as the upper boundaries of the bottom-up planetary formation scenarios such as the core accretion, and pebble accretion is still unknown. Furthermore, although the previous studies did not consider the selection effects of the planet detections, the detection limits of the radial velocity measurements clearly depend on the metallicity of the host star (see Figure 1 (a)).

Here, we report that 623 samples comprising gaseous planets and brown-dwarfs are divided into three-mass regimes with boundary masses of 4 and $20 M_J$. The upper boundary mass is thought to represent the upper mass limits of planetary objects formed around G-type and early-type stars. The lower boundary mass represents a difference between the planetary formation processes around G-type and early-type stars. While most of the samples orbiting the G-type stars are naturally ex-

plained by the core accretion model, the samples more massive than $4 M_J$ orbiting early-type stars seem to be formed by the disk instability process, where the G-type and early-type stars were defined as stars with masses ranging from 0.8 to $1.3 M_\odot$, and more larger than $1.3 M_\odot$ in this paper, respectively. Note that the samples constructed for this study were considered such that an impact of the selection effect of the radial velocity on statistical analysis is minimized.

This paper is organized as follows. In Section 2, we explain how the samples applying to statistical analysis were constructed, introducing “common-biased samples” that were selected such that an impact of the difference between the selection effects in the metal-rich and -poor regions on the analysis is minimized. In Section 3, we derive the boundary metallicity that is divided into two regions such that the distributions of the planet masses and semi-major axes are most different. We also show that the samples are divided into three-mass regimes through applying the Gaussian mixture model to the samples and three-mass regimes arise from the difference between the distributions for gaseous objects orbiting G-type and early-type stars. In Section 4, we discuss what the upper-mass limit of the gas giants formed via the bottom-up planetary formation is and whether the disk-instability-induced planetary formation occurs, comparing the results of the statistical analysis with the two planetary formation models.

2. METHOD

In this section, we explain how to perform statistical analysis for extrasolar gaseous objects to understand their formation and evolution processes and show how to deal with the selection effect of radial velocity measurements by which the samples constructed for this study were detected. We also explain how we constructed the samples, determining the boundary between gas dwarfs such as Neptune-like planets and gaseous giants.

2.1. Overview of Statistical Analysis

In this study, we first examined whether the difference between the distributions of semi-major axes and masses for gaseous objects orbiting metal-rich and -poor stars arises from the selection effect of radial velocity measurements or from the dependence of the planetary formation and evolution process on the disk metallicity, constructing samples named as “common-biased samples” that minimize an impact of the selection effect on the distributions, as to be discussed in Section 2.2. Given that the measurement errors follow a normal distribution, we sampled the host-star metallicities and companion masses, and then divided the common-

biased samples into two by a host-star metallicity. Using the “anderson_ksamp” module in Python, we compared the divided sub-samples in terms of planet mass and semi-major axis with two-sample Anderson-Darling test. Calculating the p-values derived from the two-sample Anderson-Darling test as a function of the host-star metallicity, we searched for a boundary metallicity that divides the common-biased samples such that the distributions of companion masses and semi-major axes for the two sub-samples are most different. We iterated this procedure 1,000 times and finally evaluated how much different the distributions of the two common-biased sub-samples are in terms of the semi-major axis and planet mass at the boundary metallicity. This result is shown in Section 3.1.

Next, we explored how many populations exist in extrasolar gaseous objects discovered so far to investigate what the upper mass limit of the core-accreted planets is; we re-examined whether only two populations exist in the extrasolar gaseous objects, as shown in the several previous studies (Ribas & Miralda-Escudé 2007; Santos et al. 2017; Schlaufman 2018). Using the “GaussianMixture” package in Python, we applied two-dimensional Gaussian mixture model to the diagram of host-star metallicities versus companion masses for the common-biased samples. The number of the Gaussian mixture models used for this cluster analysis ranges from 1 to 10. We determined the number of the components of the best Gaussian mixture model based on the Bayesian Information Criterion as well as to which cluster each common-biased sample belong. Sampling the host-star metallicities and companion masses, we repeated this procedure 1,000 times. This result is introduced in Section 3.3.

2.2. Common-biased Samples

In order to reveal the distributions of masses and orbital properties for samples orbiting various host-star metallicities, we gathered extrasolar gaseous objects discovered by radial velocity observations that can precisely determine lower limit of companion mass, semi-major axis and eccentricity. The gathered objects were referred to as “original samples” in this paper. Considering that there exists the relation between the planetary-formation processes and the host-star metallicity, as introduced in Section 1, it is preferable that the accuracies and terms of the radial velocity measurements, which detected the original samples, are independent of the host-star metallicity. This is because the original samples detected via radial velocity measurements are influenced by two selection effects: (i) limited sensitivity to long-period planets owing to short observation terms

and (ii) limited sensitivity to low-mass planets owing to a lack of measurement precision in radial velocity measurement. The maximum semi-major axis, $a|_{max}$, and lower mass limit, $M_p \sin i|_{min}$, of the detectable companion can be determined by the accuracy, σ , and term, τ , of the radial velocity measurements as below (Torres et al. 2008),

$$a|_{max} = M_*^{\frac{1}{3}} \tau^{\frac{2}{3}}, \quad (1)$$

$$M_p \sin i|_{min} \approx 4.919 \times 10^{-3} P^{\frac{1}{3}} (1 - e^2)^{\frac{1}{2}} M_*^{\frac{2}{3}} \sigma, \quad (2)$$

where, M_* , P , e , and i are the host-star mass, the orbital period, eccentricity and orbital inclination of the companion, respectively. The region in which a companion can be detected was derived for each radial velocity measurement based on Equation (1) and (2). Figure 1 (a) compares detection probabilities of a companion with radial velocity measurements of all the samples, early-type, and G-type stars in the metal-rich and -poor regions in terms of the semi-major axis and lower mass limit. Note that the boundary metallicity was fixed to 0 dex. As shown in Figure 1, the accuracies of the radial velocity measurements for the metal-poor original samples are clearly worse than those for the metal-rich ones. The detectable semi-major axes for the original samples orbiting the metal-rich stars are almost same as those of the metal-poor samples. Thus, the selection effect of the radial velocity measurements depends on the host-star metallicity and affects the distributions of masses and semi-major axes for the two original sub-samples orbiting the metal-rich and -poor samples.

Focusing on a fact that the distributions of masses and semi-major axes for the original samples discovered in the metal-rich (-poor) region are biased with the selection effect of the radial velocity measurements for the metal-rich (-poor) stars, we can minimize the impact of the difference between the selection effects in the metal-rich and -poor regions on the original samples through filtering the metal-rich (-poor) original samples with the selection effect in the metal-poor (-rich). The selection biases of the samples orbiting the metal-rich and -poor stars were equalized (see Figure 1 (b)). In the filtering process, we judged whether each original sample simply satisfies the following criteria:

$$M_{p,j} \sin i_j - M_{p,k} \sin i_k|_{min} \geq \frac{1}{2} (a_j - a_k|_{max}), \quad (3)$$

$$a_j \leq a_k|_{max}, \quad (4)$$

where j and k represent the j -th original sample and the k -th radial velocity observation, respectively. Note that the j -th original sample is observed by the randomly selected k -th radial velocity observation for each iteration.

Each original sample is included in the filtered samples only when the above criteria are satisfied. Now, we refer the filtered samples to as “common-biased samples.”

2.3. Preparation of Samples

The original samples considered in this study were limited to companion objects detected by the radial velocity observations, allowing the orbital parameters to be characterized and lower limit of companion mass to be determined. Essentially, the original samples were selected from those labeled “Radial Velocity” in the “detection method” column of the Extrasolar Planet Encyclopedia catalog as of the end of June 2018 (Schneider et al. 2011). The radial velocities of the host stars orbited by the original samples, and the orbital periods and eccentricities of the original samples were also collected from the same catalog. The SWEET-Cat catalog was referred to for the metallicity and mass of the host star (Santos et al. 2013; Sousa et al. 2018); this catalog presents the uniformly derived stellar parameters of the planet host stars. For some of the original samples that are not listed in the SWEET-Cat catalog, the metallicities and masses compiled in the Geneva-Copenhagen catalog (Casagrande et al. 2011) was applied and calibrated by using regression lines for G-type and early-type stars. The regression lines was determined from the metallicity or mass correlation between the SWEET-Cat and Geneva-Copenhagen catalogs to minimize measurement biases for host-star metallicities and masses (see Figure 2). Note that 41 and 4 samples orbiting the G-type and early-type stars were, respectively, calibrated in terms of the host-star metallicity. Using the stellar mass and the lower limit of companion mass was newly calculated based on Equation (2) because the host-star masses were revised.

The measurement accuracy and observation term for the radial velocity measurement of each original sample as the indicators of the selection effect were extracted from the exoplanets.org catalog. According to the Kepler’s third law shown in Equation (1), the observation term and host-star mass provide the upper limit on the semi-major axis of a detectable companion with each radial velocity measurement. Using the derived maximum semi-major axis, host-star mass and measurement accuracy, the lower mass limit of the detectable companion was derived based on Equation (2).

2.4. Boundary between Gas Giants and Neptune-like Planets

Only gaseous objects were extracted from all the samples in the Extrasolar Planet Encyclopedia catalog to remove the impact of low-mass samples, such as Neptune-mass planets (gas dwarfs) and super-Earths, on this

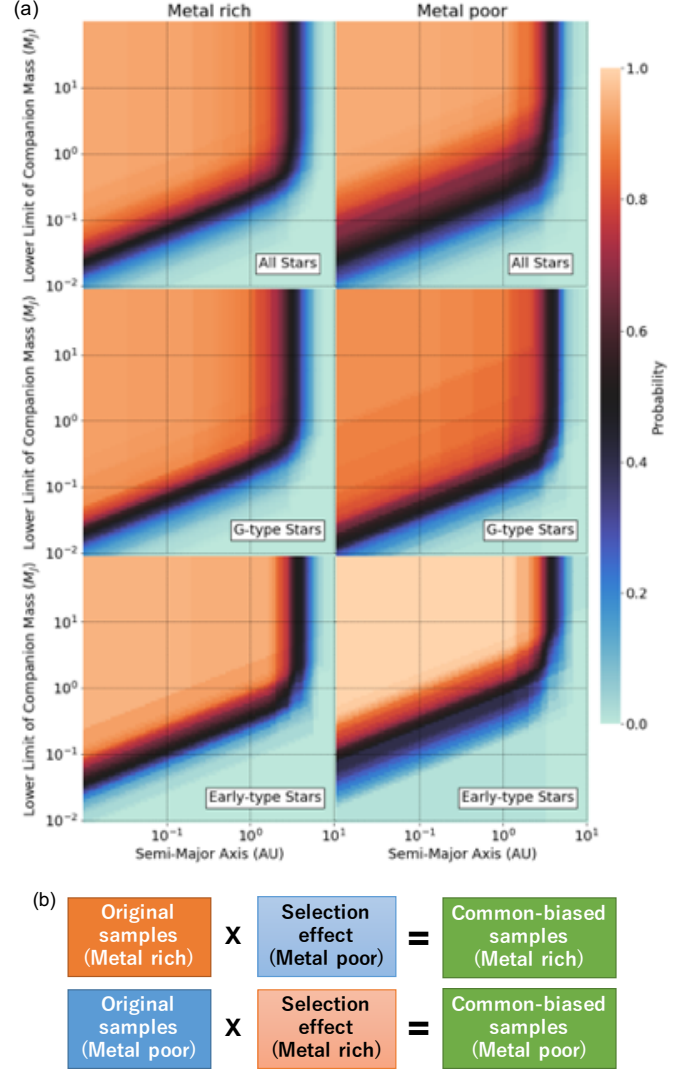


Figure 1. (a) Detection probabilities of a companion with the radial velocity measurements of all stars (upper panel), G-type stars (middle panel), and early-type stars (lower panel) in the metal-rich (left column) and -poor regions (right column) in terms of semi-major axis and companion mass. 0 dex was applied as the metallicity boundary. The probability was defined as the fraction of the number of the radial velocity measurements that can detect a companion to the total of the measurements in each metallicity region. Note that the G-type and early-type stars were, respectively, defined as stars with masses ranging from 0.8 to 1.3 M_{\odot} and ones more massive than 1.3 M_{\odot} in this paper. (b) Procedure for equalizing the selection biases included in the original samples in two different metallicity regions. The original metal-rich (-poor) samples were additionally filtered with the selection effect constructed from the radial velocity measurements of the metal-poor (-rich) original samples. The filtered original samples were defined as “common-biased samples” that are biased by a common selection effect. The filtering procedure judges whether the original samples can be detected by radial velocity measurements with the constructed selection effect, and the filtered samples are included in the common-biased samples only when the original samples are detectable.

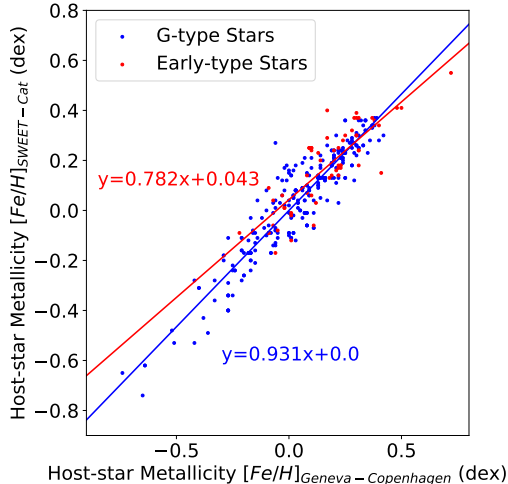


Figure 2. Metallicity correlations between the SWEET-Cat and Geneva-Copenhagen catalogs for G-type (blue) and early-type stars (red). The numbers of samples in both the catalogs are 271 for G-type stars and 58 for early-type stars. y and x in the linear regression equations represent the host-star metallicities of the SWEET-Cat and Geneva-Copenhagen catalogs, respectively.

analysis. We determined the boundary mass between the gaseous and gas-dwarf objects from a perspective of both theory and observation. According to a previous study (Ida & Lin 2004a), gas-dwarf objects, which primarily consist of heavy-core objects such as Neptune and Uranus, have the potential to grow to the extent allowed by the core building materials inside their semi-major axes. This growth occurs via giant impacts in the inner region of the disk after the disk gas dissipates. However, this core growth is limited by the scattering effect of the heavy core increasing with greater distances from the central star. Therefore, the mass of a gas-dwarf object reaches a maximum at the semi-major axis, where the scattering effect begins to limit the core growth. Given that the ratio of collision-to-ejection probabilities for the heavy core is 0.1 and the core density is 1 g/cm^3 , the upper mass limit of the gas-dwarf object is approximately $0.1 M_J$ for dust surface densities of 3 times the Minimum Solar Nebulae Model value (MMSN).

From a standpoint of the observation, a boundary between gas giants and gas dwarfs at four times the Earth’s radius has been observationally revealed by the Kepler data (Buchhave et al. 2012). From the empirical planetary mass-radius relation (e.g., Bashi et al. 2017):

$$\frac{R_p}{R_\oplus} \propto \left(\frac{M_p}{M_\oplus} \right)^{0.55 \pm 0.02}, \quad (5)$$

we found that the boundary of planetary mass is about 30 times the Earth’s mass, corresponding to $0.1 M_J$. Based on these considerations, $0.1 M_J$ was applied in this study as the boundary mass between gas giants and gas dwarfs. The numbers of samples and their planetary systems considered in this study are 623 and 520, respectively.

3. RESULTS

In this section, we quantitatively show how different the distributions of the orbital properties and planet masses for the extrasolar gaseous objects orbiting the metal-rich and -poor stars are, minimizing the impact of the selection effect of radial velocity measurement on their distributions. We also explore how many components exit in the extrasolar gaseous objects through classifying the common-biased samples with the Gaussian mixture model.

3.1. Metallicity Boundary for Common-Biased Samples

We first determined the metallicity boundary that divides the original samples into two such that the distributions of planet mass and semi-major axis in the two metal-rich and -poor regions are most different, respectively, considering the selection effect of the radial velocity measurements, as explained in Section 2.1. Figure 3 shows the p-values derived by the two-sample Anderson-Darling test for the distributions of the semi-major axes and lower mass limits of the common-biased samples, changing the metallicity boundary from -0.7 to 0.4 dex. We iterated the calculation 1,000 times and averaged the calculated p-values for each divided point to derive the mean and standard deviation of the p-values. The minimum p-values of the two-sample Anderson-Darling tests for the distributions of the semi-major axis and the planet mass were 2.4×10^{-3} and $3.5 \times 10^{-5}/4.2 \times 10^{-5}$ at the metallicity of -0.04 and -0.29/-0.06 dex, respectively. Thus, we found that the planetary distributions in the metal-rich and -poor regions do not arise from the selection effect of the radial velocity measurements but from the planet formation and evolution. In this study, we used applied -0.05 dex as the metallicity boundary for constructing the common-biased samples, considering that the two minimum p-values are around -0.05 dex.

Next, as shown in Figure 4, we compared the distributions of semi-major axes and lower limits of companion mass for the common-biased sub-samples in the metal-rich and -poor regions that were divided by the boundary metallicity of -0.05 dex. The samples with semi-major axes less than 0.3 AU and masses larger than

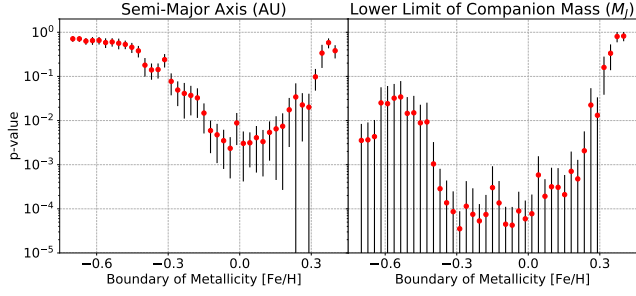


Figure 3. P-values calculated via two-sample Anderson-Darling tests for the semi-major axis (left) and the lower limit of the companion mass (right) of the original samples as a function of the metallicity boundary. The red points and black vertical bars represent the mean p-values and their standard deviations, respectively. The number of the calculations for each metallicity boundary is 1,000.

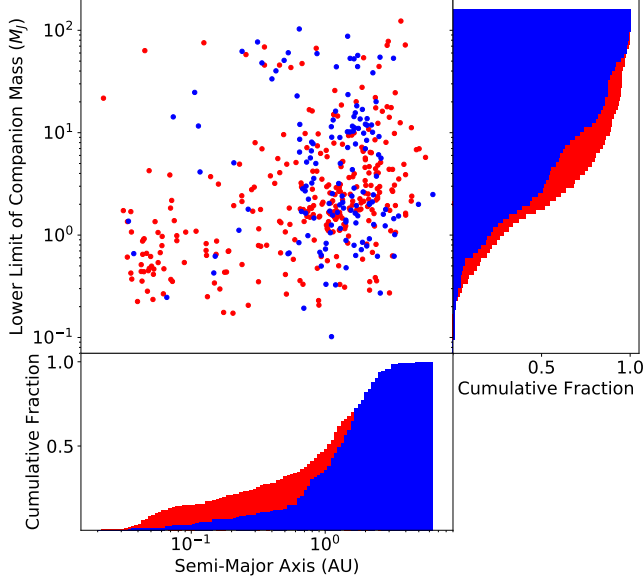


Figure 4. Distribution of semi-major axes and lower limits of companion mass for the common-biased samples (upper left) and the cumulative distributions of semi-major axis (bottom) and lower limit of companion mass (right). The red and blue points/bins represent the metal-rich and -poor samples, respectively. An example among the 1,000 calculations was shown.

about 5 M_J in the metal-poor region are relatively lack and excess compared to those in the metal-rich region, respectively. In Section 3.3, we discuss where the difference between the planetary distributions in the metal-rich and -poor regions comes from.

3.2. Three-Mass Regimes of Gaseous Objects

We classified the common-biased samples selected from the 623 original ones in a diagram of the host-star metallicity and companion mass with the Gaussian mixture model to explore how many sub-samples exist in the extrasolar gas giants discovered to data, given that each sub-sample follows a normal distribution. Changing the number of the sub-samples, we evaluated each model with the Bayesian Information Criterion and found that the three-component model is suitable as the best Gaussian mixture model for the common-biased samples. Figure 5 shows the best suited model for the common-biased samples. The common-biased samples are divided into three almost along two boundary masses of 4 and 20 M_J . The three-component model results from relative paucity of the common-biased samples in two specific regions in the diagram of host-star metallicity versus companion mass; the two regions indicate gaseous objects with masses ranging from 20 to 30 M_J around both the metal-rich and -poor stars and those with masses ranging from 0.1 to 4 M_J around the metal-poor stars. As a result, the mean metallicity of the stars hosting the gaseous objects more with masses from 4 to 20 M_J is lower than that of the samples lighter than 4 M_J and the mean metallicity of the samples more massive than 20 M_J is much lower than those of the other two sub-samples. Thus, we also confirmed that the lower boundary mass is consistent with the results shown in the previous studies (Ribas & Miralda-Escudé 2007; Santos et al. 2017; Schlaufman 2018).

3.3. Planetary distributions around G- and early-type stars

We next extracted the sub-samples orbiting G-type stars with masses ranging from 0.8 to 1.3 M_\odot and early-type stars more massive than 1.3 M_\odot from the common-biased samples, and then investigated the distributions of host-star metallicities and companion masses around the two types of host-stars. Figure 6 shows the distributions of host-star metallicities for the three-mass regimes of the G-type and early-type stars. Note that the common-biased sub-samples for G-type and early-type stars were constructed by the selection biases for the two spectral-type stars shown in the middle and lower panels of Figure 1 (a).

Regarding the distribution of host-star metallicity around the G-type stars, the mean metallicities for the gaseous samples lighter than 20 M_J are much higher than that of the samples more massive than 20 M_J , which almost corresponds to that of the nearby G-type stars selected from the Geneva-Copenhagen catalog (Casagrande et al. 2011). There is also no boundary at 4 M_J in terms of the distribution of the host-star

metallicity. While a stellar formation process such as gravitational core collapse and fragmentation of molecular clouds (Padoan & Nordlund 2004; Hennebelle & Chabrier 2008) forms the gaseous objects more massive than $20 M_J$, the gaseous objects with masses ranging from 4 to $20 M_J$ as well as from 0.1 to $4 M_J$ are thought to be formed via core-accretion. Thus, the larger boundary of around $20 M_J$ clearly reflects the upper mass limit of the core-accreted planets, which are almost consistent with those shown in the previous theoretical studies (e.g., Tanigawa & Ikoma 2007; Mordasini et al. 2009; Tanigawa & Tanaka 2016). Note that the paucity of samples more massive than $20 M_J$ around the early-type stars also seems to support that the upper boundary corresponds to the maximum mass of the planetary objects.

In contrast, regarding the distribution of host-star metallicities and companion masses around the early-type stars, the mean metallicity for the gaseous objects with masses ranging from 4 to $20 M_J$ is much lower than that of the samples lighter than $4 M_J$. Therefore, the lower boundary mass of $4 M_J$ in the three-mass regimes indicates that the distribution of the host-star metallicity largely changes at the boundary of $4 M_J$ around the early-type stars. The lower boundary also reflects a difference between the planetary formation processes around the G-type and early-type stars, considering that there is no boundary at $4 M_J$ around the G-type stars. In fact, although the common-biased sub-samples with masses ranging from 4 to $20 M_J$ orbiting the G-type and early-type stars distribute in the outer region than 0.3 AU (Figure 4), their eccentricity distributions are largely different, as shown in Figure 6. Note that, because 41 and 2 samples among 380 G-type and 189 early-type stars were calibrated in terms of the host-star metallicity, respectively, the impact of non-uniformity in the samples on the distribution of host-star metallicities is small.

Based on the above considerations, we redefined the samples lighter than $20 M_J$ as planetary-mass objects and labeled the two sub-samples with masses from 0.1 to $4 M_J$ and from 4 to $20 M_J$ as “intermediate-mass planets” and “massive planets,” respectively. In addition, the samples more massive than $20 M_J$ are labeled as “brown-dwarfs.” Note that the boundary between planetary mass and brown dwarf objects established by the deuterium-burning minimum mass of around $10 M_J$ is semantic (Chabrier et al. 2014); this boundary has no physical meaning from the perspective object evolution.

4. DISCUSSION

In this section, we first discuss the formation process of the intermediate-mass and massive planets orbiting

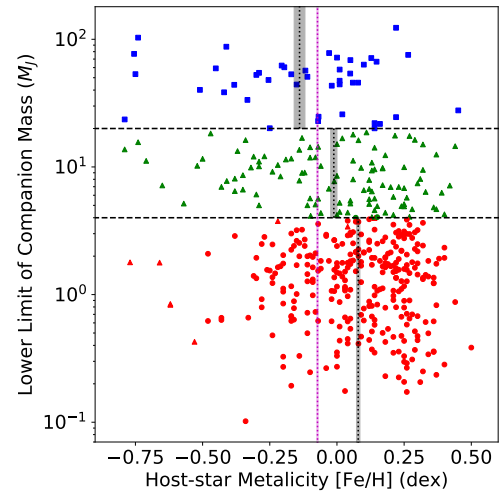


Figure 5. Distribution of host-star metallicities and lower limits of companion mass for three common-biased sub-samples classified by the best Gaussian mixture model. The different symbols of square, triangle, and circle represent the classified sub-samples. The three colors of the samples correspond to three-mass regimes with two boundary masses of 4 and $20 M_J$ shown by the horizontal long-dashed lines. The vertical short dashed line and gray region in each mass regime represent the mean metallicity and its standard deviation over 1000 iterations, respectively. The distribution of the samples in terms of host-star metallicity and lower limit of companion mass shows an example among the 1000 calculations. The magenta dashed line and region, respectively, show the mean metallicity and its standard error for all the samples in the Geneva-Copenhagen catalog, where the mean metallicity was converted with the linear regression between the samples in the SWEET-Cat and that catalogs

the G-type stars, comparing the mass distribution with that predicted by the core accretion model. We next focus on the distributions of masses and eccentricities for the intermediate-mass and massive planets orbiting the early-type stars. We finally show an entire view of the extrasolar gaseous objects discovered so far from a standard point of the two planetary formation scenarios.

4.1. Planetary Formation Process around G-Type Stars

We compared the intermediate-mass and massive planets with the simulation data generated by Mordasini et al. (2012) that performed a population synthesis around $1 M_\odot$ within the framework of the core accretion model including planet growth and migration through planet-disk interaction. The upper panel of Figure 8 shows the distributions of semi-major axes and masses for the common-biased intermediate-mass and massive planets and the simulation samples in the metal-rich and -poor regions. The distribution of semi-

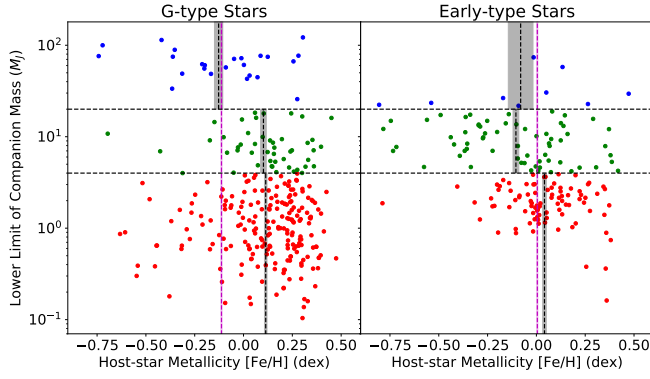


Figure 6. Distributions of host-star metallicities and companion masses for the common-biased samples orbiting G-type stars with masses ranging from 0.8 to 1.3 M_{\odot} (left) and early-type stars with masses more massive than 1.3 M_{\odot} (right). The symbols are same as those in Figure 5. The common-biased samples for G-type and early-type stars were constructed by the selection effects of the radial velocity measurements for the two spectral-type stars shown in the middle and lower panels of Figure 1, (a).

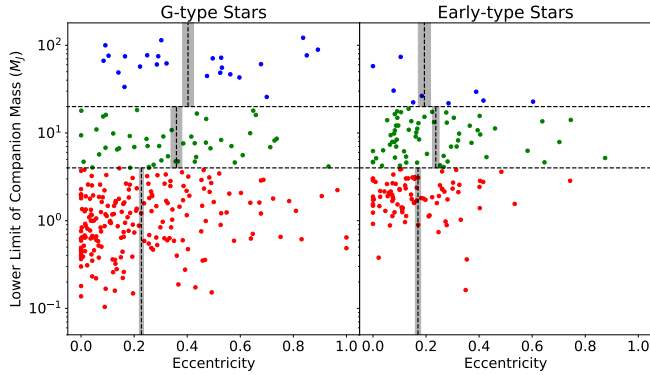


Figure 7. Distributions of eccentricities and masses for the common-biased samples orbiting G-type (left) and early-type stars (right). The symbols and lines are same as those in Figure 5.

major axes and masses for the intermediate-mass and massive planets around G-type stars are almost consistent with that for the simulation samples. In fact, as shown in the lower panel of Figure 8, the mean masses for the observation around G-type stars and simulation samples have a good agreement over the entire metallicity region. Note that the simulation samples were also filtered by both the selection effects of metal-rich and -poor regions, and the observational samples were restricted to the intermediate-mass and massive planets orbiting host stars with masses ranging from 0.8 to 1.3 M_{\odot} .

An increase in eccentricities of the massive planets orbiting G-type stars shown in Figure 7 can be also explained by the following two models that were expanded from the core accretion model. One is planet-disk interaction at Lindblad and co-rotation resonances prior to gas dissipation (e.g., Goldreich & Sari 2003). According to the numerical simulations performed by Kley & Dirksen (2006), the minimum planet mass for changing the disk gas into a high eccentricity state is 3 M_J for the viscous coefficient of 10^{-5} , which is almost consistent with the boundary between the intermediate-mass and massive planets. Another is dynamical instability induced by two closely separated gas giants and three gas giants, so called gravitational planet-planet interaction (e.g., Ida et al. 2013). The dynamical instability produces a gas giant with an eccentric orbit in outer region and a circular hot Jupiter in inner region through tidal circularization (e.g., Rasio & Ford 1996). In fact, a paucity of the intermediate-mass planets that locate within 0.1 AU around the metal-poor G-type stars was confirmed; the gravitational planet-planet interaction is thought to occur only around the metal-rich G-type stars. The previous observations also confirmed that hot Jupiters orbit only the metal-rich G-type stars (Dawson & Murray-Clay 2013; Adibekyan et al. 2013).

Thus, the distributions of masses and eccentricities for the intermediate-mass and massive planets orbiting G-type stars can be naturally explained by the core accretion model. Their distributions support that the upper mass limit of the core-accreted planets is around 20 M_J .

4.2. Planetary Formation Process around Early-Type Stars

Considering the mean host-star metallicity for the intermediate-mass planets orbiting early-type stars is relatively higher than that for the massive planets, the intermediate-mass planets are thought to be formed by core accretion. In contrast, the massive planets around early-type stars seem to preferentially orbit the metal-poor stars. Note that the mean value of the nearby early-type stars extracted from the Geneva-Copenhagen Catalog may be higher than the true value because of a systematic offset between the Geneva-Copenhagen and SWEET-Cat catalogs. In addition, the distribution of semi-major axes and masses for the massive planets around early-type stars is not consistent with that for the simulation samples; there is an excess of the massive planets orbiting metal-poor stars and most of the planets locally distribute in the transition between 1 and 3 AU, in which the simulation samples are paucity. The excess of massive planets orbiting metal-poor early-type stars differs from that expected from the core accretion

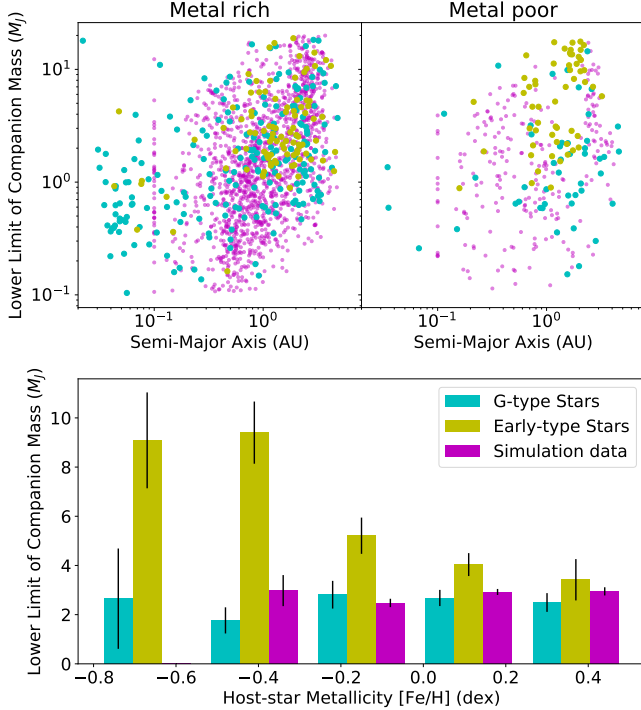


Figure 8. *Top:* Distributions of semi-major axes and lower limit of companion masses for the common-biased samples with masses less than $20 M_J$ orbiting G-type stars with masses ranging from 0.8 to $1.3 M_\odot$ (cyan dots) and early-type stars more massive than $1.3 M_\odot$ (yellow dots) and the simulation samples with masses ranging from 0.1 to $20 M_J$ (purple dots) generated by Mordasini et al. (2012) in the metal-rich (upper left) and -poor regions (upper right). *Bottom:* Histograms of mean masses for the simulation samples (purple bars) and the common-biased samples with masses less than $20 M_J$ orbiting G-type stars (cyan bars) and early-type stars (yellow bars).

formation theory in terms of the following two points. While more massive planets are likely to be formed around more metal-rich stars (Mordasini et al. 2012), the mean masses for the intermediate-mass and massive planets orbiting early-type stars clearly increases as the metallicity decreases (Figure 8). In addition, although a continuous decrease in the mass function of massive planets is theoretically predicted (Mordasini et al. 2009), the observation samples orbiting metal-poor early-type stars are clustered around 4 and $10 M_J$ (Figure 8). The eccentricities of the massive planets orbiting early-type stars also differ from those around the G-type stars (Figure 7); the eccentricities of the massive planets around the early-type stars do not seem to be enhanced through the planet-disk interaction prior to gas dissipation and gravitational planet-planet interaction. Thus, the distributions of masses and eccentricities for the massive

planets orbiting early-type stars are unlikely to be explained by the bottom-up models.

An explanation for the excess massive planets orbiting metal-poor stars is that the disk instability acts in the vicinity of metal-poor stars, because a lower mass limit applies for planets formed via the disk instability mechanism (i.e., corresponding to an order of the Jeans mass (Matsuo et al. 2007; Mayer 2010)). As a result, a sharp increase appears in the planetary mass function around $4 M_J$. It is also accepted that planet formation due to disk instability tends to occur in the vicinity of metal-poor stars because the cooling timescale in the disk mid-plane is reduced owing to low disk opacity (Cai et al. 2006; Durisen et al. 2007). The low eccentricities of the massive planets orbiting the early-type stars are also consistent with the numerical simulations (Mayer et al. 2004; Mayer 2010; Boss 2011) and the eccentricities of four gas giants orbiting HR8799, an A-type star, (Wertz et al. 2017). Note that the four gas giants are located in a region beyond the core accretion model Figure 9.

4.3. Planetary Formation Scenarios

Based on the above considerations, we compared the distribution of host-star metallicities and companion masses for the common-biased samples selected from the 623 original ones with the regions expected from the core accretion and disk instability models for the G-type and early-type stars (Figure 9). The scarce regions appear in terms of companion mass, those at 0.1 to $0.3 M_J$ and 20 to $30 M_J$ around G-type stars and those at 0.1 to $1 M_J$ and in larger than $20 M_J$ around early-type stars. The lack of the lighter planets orbiting G-type and early-type stars arises from the rapid gas accretion onto the core. In contrast, the lack of the massive companions around G-type stars represents a gap between binary star and planet formation. In addition, few brown dwarfs around the early-type stars may support that the boundary mass of around $20 M_J$ corresponds to the maximum mass of planetary objects. Thus, the lower and upper boundaries of the two regions reflect the lower and upper mass limits of extrasolar gaseous objects that are formed by the planetary formation processes, respectively. In fact, the upper mass limit is almost consistent with the theoretical expectations (Tanigawa & Ikoma 2007; Mordasini et al. 2009; Tanigawa & Tanaka 2016).

While the intermediate-mass and massive planets orbiting G-type stars can be explained by the core accretion model, the excess of massive planets around early-type stars is likely to be explained not by the bottom-up scenario but by the top-down one such as gravitational instability. The previous observational studies on dual

planetary formation scenarios (Ribas & Miralda-Escudé 2007; Santos et al. 2017; Schlaufman 2018) showed that there exists a boundary mass of 4 to 10 M_J in the diagram of host-star metallicities and masses for gaseous objects and mentioned that the boundary reflects the transition between the two planetary formations; the

upper limit of the core-accreted planets is around 4 M_J . However, we found that the boundary of 4 M_J reflects a population that is likely to be formed via disk instability and expected that planets with masses up to 20-30 M_J can be continuously formed by core-accretion around G-type stars.

REFERENCES

- Adibekyan, V. Z., Figueira, P., Santos, N. C., et al. 2013, *A&A*, 560, A51
- Bashi, D., Helled, R., Zucker, S., & Mordasini, C. 2017, *A&A*, 604, A83
- Boss, A. P. 1997, *Science*, 276, 1836
- Boss, A. P. 2002, *ApJL*, 567, L149
- Boss, A. P. 2011, *ApJ*, 731, 74
- Buchhave, L. A., Latham, D. W., Johansen, A., et al. 2012, *Nature*, 486, 375
- Cai, K., Durisen, R. H., Michael, S., et al. 2006, *ApJL*, 636, L149
- Casagrande, L., Schönrich, R., Asplund, M., et al. 2011, *A&A*, 530, A138
- Chabrier, G., Johansen, A., Janson, M., & Rafikov, R. 2014, *Protostars and Planets VI*, 619
- Chiang, E. I., Fischer, D., & Thommes, E. 2002, *ApJL*, 564, L105
- Dawson, R. I., & Murray-Clay, R. A. 2013, *ApJL*, 767, L24
- Dodson-Robinson, S. E., Veras, D., Ford, E. B., & Beichman, C. A. 2009, *ApJ*, 707, 79
- Dupuy, T. J., & Liu, M. C. 2011, *ApJ*, 733, 122
- Durisen, R. H., Reipurth, V., Jewitt, K., et al. 2007, *Univ. of Arizona Press, Tucson* 951, 607-622
- Fischer, D. A., & Valenti, J. 2005, *ApJ*, 622, 1102
- Girardi, L., Bressan, A., Bertelli, G., & Chiosi, C. 2000, *A&AS*, 141, 371
- Goldreich, P., & Sari, R. 2003, *ApJ*, 585, 1024
- Hayashi, C., Nakazawa, K., & Nakagawa, Y. 1985, *Protostars and Planets II*, 1100
- Hennebelle, P., & Chabrier, G. 2008, *ApJ*, 684, 395
- Hidalgo, S. L., Pietrinferni, A., Cassisi, S., et al. 2018, *ApJ*, 856, 125
- Ida, S., & Lin, D. N. C. 2004a, *ApJ*, 604, 388
- Ida, S., & Lin, D. N. C. 2004b, *ApJ*, 616, 567
- Ida, S., Lin, D. N. C., & Nagasawa, M. 2013, *ApJ*, 775, 42
- Kalas, P., Graham, J. R., Chiang, E., et al. 2008, *Science*, 322, 1345
- Kley, W., & Dirksen, G. 2006, *A&A*, 447, 369
- Kuiper, G. P. 1951, *Proceedings of the National Academy of Science*, 37, 1
- Lagrange, A.-M., Bonnefoy, M., Chauvin, G., et al. 2010, *Science*, 329, 57
- Lambrechts, M., & Johansen, A. 2012, *A&A*, 544, A32
- Lee, K. J., Guillemot, L., Yue, Y. L., Kramer, M., & Champion, D. J. 2012, *MNRAS*, 424, 2832
- Ma, B., & Ge, J. 2014, *MNRAS*, 439, 2781
- Marois, C., Macintosh, B., Barman, T., et al. 2008, *Science*, 322, 1348
- Matsuo, T., Shibai, H., Ootsubo, T., & Tamura, M. 2007, *ApJ*, 662, 1282
- Mayor, M., & Queloz, D. 1995, *Nature*, 378, 355
- Mayer, L., Quinn, T., Wadsley, J., & Stadel, J. 2002, *Science*, 298, 1756
- Mayer, L., Quinn, T., Wadsley, J., & Stadel, J. 2004, *ApJ*, 609, 1045
- Mayer, L., Lufkin, G., Quinn, T., & Wadsley, J. 2007, *ApJL*, 661, L77
- Mayer, L. 2010, *Formation via Disk Instability. Formation and Evolution of Exoplanets*, by Barns, R. (eds.) Wiley, 71-99
- Mayor, M., Marmier, M., Lovis, C., et al. 2011, *arXiv:1109.2497*
- Mizuno, H. 1980, *Progress of Theoretical Physics*, 64, 544
- Mordasini, C., Alibert, Y., Benz, W., & Naef, D. 2009, *A&A*, 501, 1161
- Mordasini, C., Alibert, Y., Benz, W., Klahr, H., & Henning, T. 2012, *A&A*, 541, A97
- Ormel, C. W., & Klahr, H. H. 2010, *A&A*, 520, A43
- Padoan, N., & Nordlund, Å. 2010, *ApJ*, 617, 559
- Perri, F., & Cameron, A. G. W. 1974, *Icarus*, 22, 416
- Pollack, J. B., Hubickyj, O., Bodenheimer, P., et al. 1996, *Icarus*, 124, 62
- Rasio, F. A., & Ford, E. B. 1996, *Science*, 274, 954
- Ribas, I., & Miralda-Escudé, J. 2007, *A&A*, 464, 779
- Santos, N. C., Israelian, G., Mayor, M., Rebolo, R., & Udry, S. 2003, *A&A*, 398, 363
- Santos, N. C., Israelian, G., & Mayor, M. 2004, *A&A*, 415, 1153
- Santos, N. C., Sousa, S. G., Mortier, A., et al. 2013, *A&A*, 556, A150

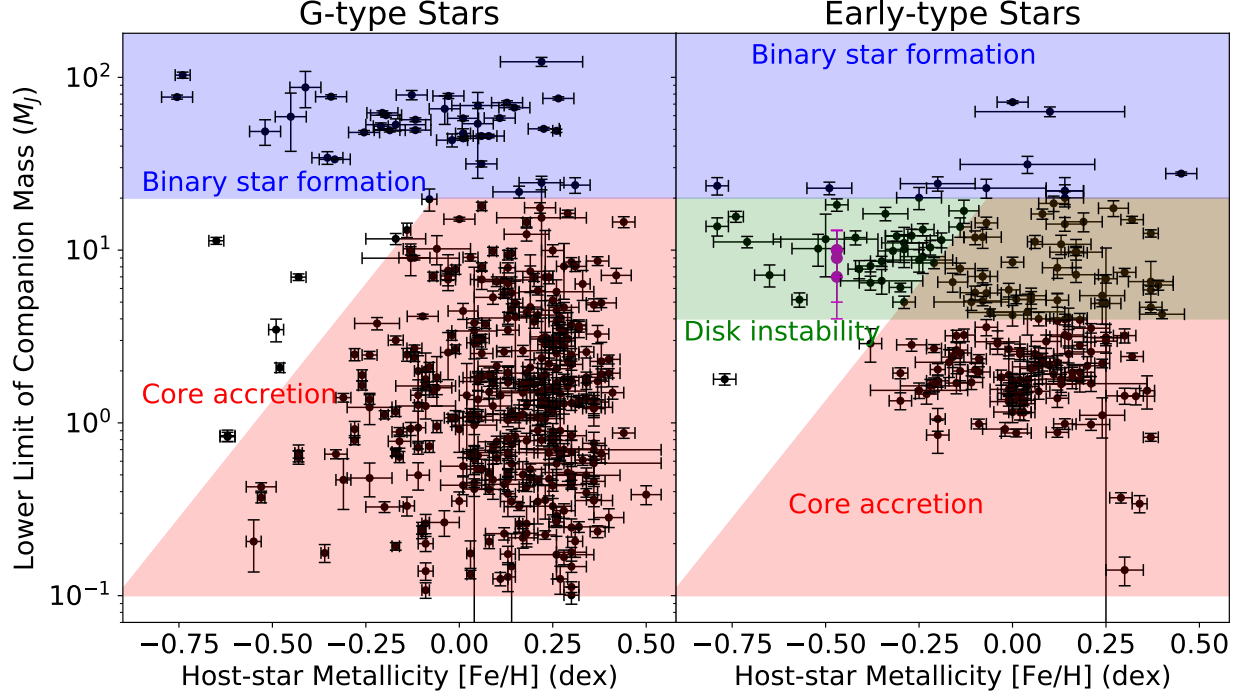


Figure 9. Distributions of host-star metallicities and companion masses for the common biases samples orbiting G-type stars (left) and early-type stars (right). The common-biased samples (black dots) and the four planets orbiting HR 8799 (purple dots) were compared with expectations from the core accretion and disk instability theories in terms of host-star metallicities and planetary mass distributions. The red, green, and blue regions indicate where the objects can be formed by core accretion, disk instability and binary star formation, respectively. The black error bars represent the 1σ measurement errors. The dependence of the maximum mass of the core-accreted planets on the disk metallicity around early-type stars was assumed to be same as that around G-type stars, which was derived from the population synthesis performed by [Mordasini et al. \(2012\)](#).

Santos, N. C., Adibekyan, V., Figueira, P., et al. 2017, *A&A*, 603, A30

Schlaufman, K. C. 2018, *ApJ*, 853, 37

Schneider, J., Dedieu, C., Le Sidaner, P., Savalle, R., & Zolotukhin, I. 2011, *A&A*, 532, A79

Sousa, S. G., Santos, N. C., Mayor, M., et al. 2008, *A&A*, 487, 373

Sousa, S. G., Santos, N. C., Israelian, G., et al. 2011, *A&A*, 533, A141

Sousa, S. G., Adibekyan, V., Delgado-Mena, E., et al. 2018, *A&A*, 620, A58

Tanigawa, T., & Ikoma, M. 2007, *ApJ*, 667, 557

Tanigawa, T., & Tanaka, H. 2016, *ApJ*, 823, 48

Torres, G., Winn, J. N., & Holman, M. J. 2008, *ApJ*, 677, 1324

Wang, J., & Fischer, D. A. 2015, *AJ*, 149, 14

Wertz, O., Absil, O., Gómez González, C. A., et al. 2017, *A&A*, 598, A83